JOURNAL OF AIRCRAFT
Vol. 48, No. 2, March–April 2011

Fluid-Structure Coupled Analysis of a Transport Aircraft and Flight-Test Validation

Stefan Keye*
DLR, German Aerospace Center, 38108 Braunschweig, Germany

DOI: 10.2514/1.C000235

The estimation of aerodynamic loads of a transport aircraft taking into account static aeroelastic deformations at steady-state flight conditions is described. Within the scope of a pilot study a fluid-structure coupled simulation approach based on state of the art numerical fluid dynamics and structural analysis methods has been applied to an Airbus A340-300 aircraft in both cruise and high-lift configurations. Coupled analyses were performed using an in-house simulation procedure linking DLR's flow solver TAU and the commercial finite element code NASTRAN™. Numerical results were validated against flight-test data generated in the research project Aircraft Wing with Advanced Technology Operation (AWIATOR) funded by the European Union. A good agreement of simulation results and flight-test data, including both fluid dynamics and structural deformation properties, was observed. Aeroelastic effects in cruise flight were found to be larger than in high-lift, where only slats and the wing's leading-edge region are affected. Work presented in this paper is part of a cooperation between DLR and Airbus Deutschland within the joint research project High-Lift Innovative Technologies.

Nomenclature

C_D	=	drag coefficient
C_L	=	lift coefficient
C_{My}	=	pitching moment coefficient
C_p	=	pressure coefficient
c	=	chord length
F	=	force
h_p	=	altitude
i	=	computational fluid dynamics face centroid number
j	=	finite element node number
M	=	moment of torsion
Ma	=	Mach number
m	=	mass
$p_{dyn.}$	=	dynamic pressure
p_s	=	static pressure
Re	=	Reynolds number
r	=	radius
v_c	=	cruising speed
w	=	wing bending deformation
x, y, z	=	Cartesian coordinates
y^+	=	nondimensional wall distance
α	=	angle of attack
β	=	yaw angle
ε	=	wing twist deformation
η	=	spanwise coordinate

I. Introduction

THE request for increasingly accurate numerical flow simulations necessitates considering the physical interaction between the elastic body and the outer flowfield, as in many applications structural deformations caused by aerodynamic loads lead to significant changes in the surrounding fluid flow and cannot be neglected. Therefore, monodisciplinary computational fluid dynamics (CFD) approaches tend to become more and more insufficient for a high-quality numerical prediction of aerodynamic performance data or the comparison of numerical and experimental results. Typical examples are modern, long-range aircraft with flexible, high aspect ratio wings, like the Airbus A340 or A380, at varying load cases, or wind-tunnel models at high Reynolds numbers and off-design flow conditions. To take into account the interaction of fluid flow and flexible structure, DLR's Reynolds-averaged Navier–Stokes (RANS) flow solver TAU [1] has recently been linked to the finite element (FE) structural analysis software NASTRAN™† to constitute a fully automated fluid-structure coupled (FSC) simulation environment. The coupling approach is designed to simulate static aeroelastic effects only. For an overview of coupling strategies for dynamic phenomena, such as flutter or buffeting, see, e.g., [2]. To this point, the new aeroelastic simulation procedure had been applied only to small-scale, generic test cases, like the 3-D LANN Wing [3] or the TC11 High-Lift Configuration used in the European Union research project EUROLIFT [4] (European High-Lift Programme), and wind-tunnel models, e.g., the DLR-F11 High-Lift Configuration, a representative wide-body commercial aircraft half-model with empennage and three-element high-lift system [5], or the DLR-F6 Wing-Body Configuration, where a stress analysis was conducted within the scope of preparing the model for a test campaign in NASA's National Transonic Facility (NTF) [6]. To demonstrate the method's capabilities to handle complex, real-life structures, the Airbus A340-300 transport aircraft was chosen, Fig. 1. Main specifications are given in Table 1. Two flight configurations were considered, the "CLEAN" wing used during high-speed cruise, and the "FULL" configuration with flaps and slats completely deployed for approach and landing. Main goals of this research are to numerically simulate the elastically deformed, fully trimmed aircraft in free flight, and to evaluate coupled analysis results accuracy by comparison to experimental data from two flight-test campaigns performed in 2003 and 2006 within the AWIATOR project using the A340-300 MSN001 aircraft.

II. Fluid-Structure Coupled Simulation Procedure

DLR's fluid-structure coupled steady state simulation procedure, Fig. 2, incorporates the in-house flow solver TAU and the computational structural mechanics (CSM) code NASTRAN™ as main components. Additional modules are a bidirectional interpolation

Presented as Paper 2009-4198 at the 39th AIAA Fluid Dynamics Conference & Exhibit, San Antonio, TX, 22–25 June 2009; received 23 December 2009; revision received 23 September 2010; accepted for publication 26 October 2010.

*Scientist, Department of Transport Aircraft, Institute of Aerodynamics and Flow Technology, Lilienthalplatz 7.

†Data available online at http://www.mscsoftware.com/products/msc_nastran.cfm [retrieved May 2008].

Fig. 1 Airbus A340-300.

routine for mapping aerodynamic loads to the structural nodes and transferring structural deflections back to the CFD mesh, and, closing the coupling loop, a volume mesh deformation algorithm.

The analysis starts from an initial RANS CFD solution, which is computed on the undeformed grid. Then, static pressure and friction coefficients along with the IDs, coordinates, and connectivity of the grid nodes, which constitute the CFD coupling surface, are transferred to the interpolation module using the Aerodynamic Mesh Interface Format (AMIF) specification.

For each surface element in the CFD grid the interpolation module computes a force vector using pressure coefficient values, cell face area, and cell orientation. Then, aerodynamic forces are mapped to the structural nodes located on the coupling surface. The corresponding finite element surface data is provided from another AMIF file and processed in the same manner. Because of the considerable resolution difference, which usually exists between CFD and structural meshes, or when, as in this case, connectivity data of the finite element surface nodes is not available, the application of a simple linear interpolation strategy is not applicable and a nearest neighbor search algorithm is used instead [5]. An assessment of both interpolation methods with respect to the coupling of aerodynamic forces between CFD and CSM meshes is provided in [7]. For a given CFD face centroid i the nearest neighboring CSM grid point j is identified and a force component $F_{j,\mathrm{CSM}}$ and associated moment $M_{j,\mathrm{CSM}} = F_{i,\mathrm{CFD}} \times r_{ij}$ are mapped to node j, Fig. 3. This procedure ensures a conservative interpolation with respect to both force and moment balance on CFD and CSM side. An example showing a computed C_p-distribution and the equivalent structural force distribution is given in Fig. 4.

Next, nodal loads from the interpolation routine are reformatted into NASTRAN™ force cards and linked to the bulk data file. A linear, static structural analysis is performed and the resulting nodal deflection components along the coupling surface are mapped back to the CFD surface mesh, Fig. 5. Because the nearest neighbor search algorithm used before is not appropriate for deformation fields, an interpolation scheme based on radial basis functions (RBF) is used [5]. The technique is particularly well suited for smooth functions [8,9], like the deformations of aerodynamic structures considered in this application.

Table 1 Airbus A340-300 specifications

Length	63.60 m (208 ft, 8 in.)
Wing span	60.30 m (197 ft, 10 in.)
Wing area	361.6 m^2 (3, 892 ft^2)
Height	16.85 m (55 ft, 3 in.)
Empty weight	129,275 kg (295,503 lb)
Maximum takeoff weight	276,500 kg (609,600 lb)
Cruising speed	Ma 0.82 (484 kn)
Range	13,700 km (7,400 NM)
Service ceiling	11,887 m (39,000 ft)
Engines	4 × CFM 56.5-C2
Thrust	138.78 kN each
Maiden flight	25 October 1991

Before a new flow solution is started, the interpolated surface nodal deflections are extrapolated into the volume mesh. This is achieved by applying the RBF interpolation functions used for the surface mesh deformation to the volume mesh nodes also. Additionally, the resulting deflections are superimposed with a weighting function based on wall distance to achieve a gradual decline of nodal deflections from the coupling surface into the flowfield and to let them vanish for a specified distance, for example along the far-field boundaries. The method is applicable to both hybrid unstructured and block-structured meshes.

Finally, a new CFD solution is computed on the deformed mesh. A typical convergence history for a fluid-structure coupled simulation is plotted in Fig. 6. The individual coupling steps are easily identified by steep increases in density residual and altered lift, drag, and pitching moment coefficient values. Iteration proceeds until user-defined convergence criteria, based on either flow or structural parameters, are accomplished.

With high-lift configurations featuring multiple aerodynamic surfaces a somewhat advanced interpolation procedure is required to ensure a correct allocation of forces to the individual components, i.e., wing, flaps, and slats, and to take into account rigid body deflections of flaps and slats with respect to the wing. This is achieved by using a component-based interpolation for both aerodynamic forces and structural deflections. For the Airbus A340-300 in FULL configuration three main groups (wing/aileron/winglet, inner/outer flaps, slats 1–7) have been defined. Aerodynamic forces on wing, aileron, and winglet are transferred to the wing box structure and forces on flap and slat surfaces are assigned to the corresponding flap and slat structures. A component-based interpolation can also assist in increasing the robustness of the nearest neighbor search algorithm, e.g., when upper and lower aerodynamic surfaces are close together and the structural data is scarce.

Additionally, forces on the flap track fairings are allocated to the respective attachment points on the flap track structures and forces on the inner and outer engine nacelles are concentrated on the engine pivot nodes. For these components the CSM coupling surfaces consist of single points (engine pivot nodes) or sets of points (fairing attachment points) only. Aerodynamic forces from the CFD mesh surfaces are interpolated directly onto these points using the standard nearest neighbor search algorithm.

Interpolation of structural deflections from the finite element model uses the wing box, flap, and slat structures as separate components for deformation of the CFD surface mesh.

For the CLEAN configuration the groups related to the deployed high-lift devices, i.e., inner/outer flaps and slats 1–7, are omitted. Here, the flaps and slats are an integral part of the wing and are included in the respective interpolation component. Loads on flap track fairings and engine nacelles are interpolated in the same way, as with the FULL configuration.

III. Numerical Models

The CAD surface geometry used for the A340-300 flow simulations is based on a half-model of fuselage, main wing, leading-edge slats, trailing-edge flaps, flow-through engine nacelles, pylons, and horizontal and vertical stabilizers. For the CLEAN wing configuration and flight conditions a suitable mesh with 9.5 million nodes was readily available from the DLR research project HighPerFlex (High-Performance Flexible Aircraft, 2004–2006). To ensure good deformability using the deformation algorithms available at that time the mesh was built using a low tetrahedra aspect ratio of ≤ 2.0. Aside from the resulting higher total number of cells no tradeoffs regarding mesh deformation qualities, e.g., with respect to numerical and physical accuracy or near-wall refinement procedures, were involved. For the high-lift configuration an unstructured, hybrid CFD mesh comprising a total of 26.8 million grid nodes, Fig. 7, was generated using the grid generation software CENTAUR[‡]. The hybrid mesh consists of

[‡]Data available online at http://www.centaursoft.com/ [retrieved May 2008].

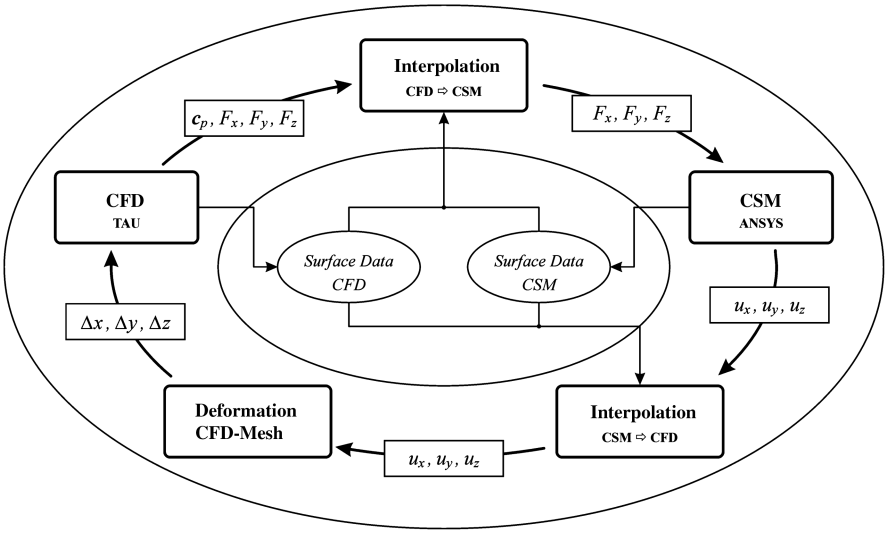

Fig. 2 Simulation procedure for fluid-structure coupled analyses.

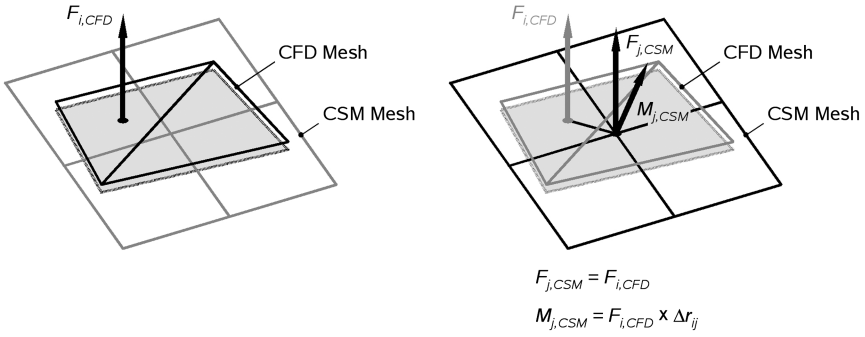

Fig. 3 Force mapping between CFD and CSM meshes.

prism elements in the boundary-layer regions and tetrahedra and pyramids in the outer flowfield. Owing to recent improvements in the mesh deformation algorithm, the high-lift grid did not require particular treatment with respect to deformability. The nondimensional wall distance targets for both meshes were $y^+ = 1$. Table 2 lists the estimated accuracies with respect to lift, drag, and pitching moment coefficients.

CFD simulations were performed using an implicit backward-Euler time stepping scheme, a 4w multigrid cycle with LU-SGS smoother, and Runge–Kutta relaxation solver. Turbulence was modeled using a one-equation Edwards-modified Spalart–Allmaras model, which is considered a good compromise between accuracy and computing time. Detailed information on the algorithms, solvers, and turbulence models available within the TAU code is provided in [10].

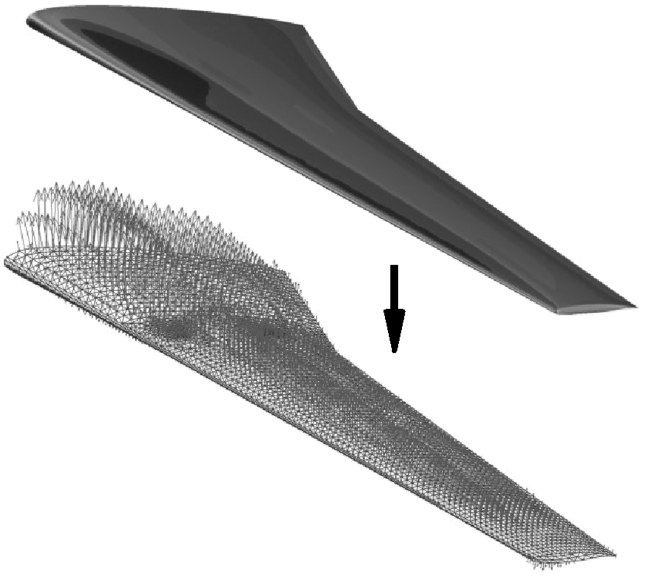

Fig. 4 Computed C_p-distribution (top) and interpolated structural forces (bottom).

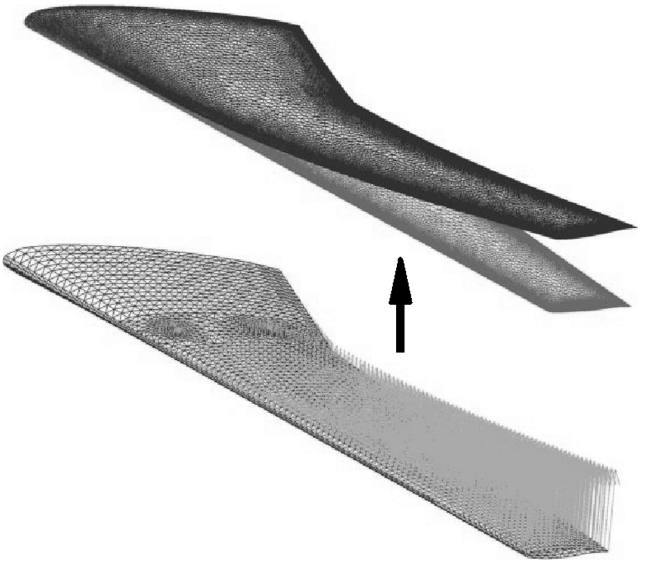

Fig. 5 Computed structural deflections (bottom) and deformed CFD surface mesh (top); deflections not to scale.

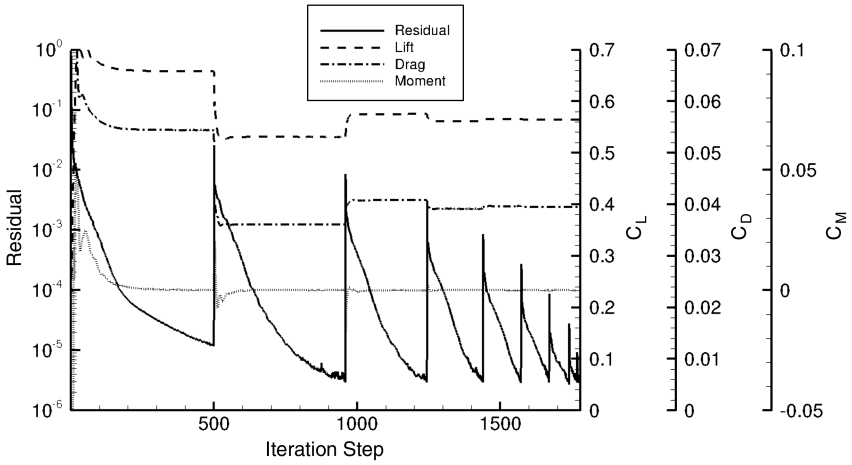

Fig. 6 Coupled simulation convergence history.

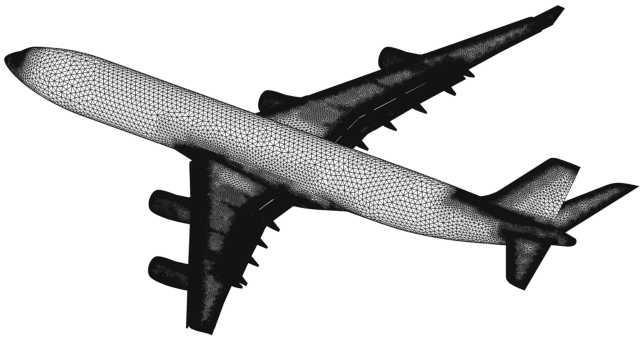

Fig. 7 CFD surface mesh, FULL configuration.

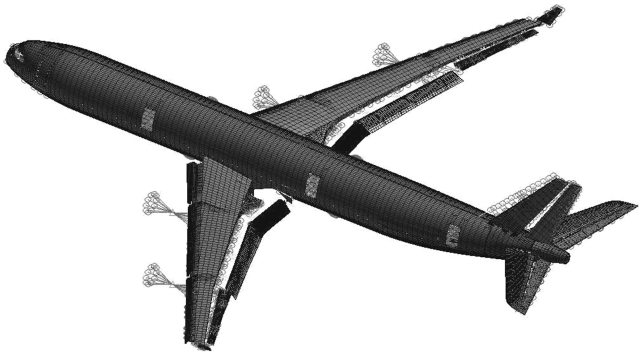

Fig. 8 Finite element model, FULL configuration.

To ensure correct aerodynamic wing loads all uncoupled and coupled flow simulations were run at constant C_L with the aircraft trimmed for $C_{My} \equiv 0$ for the given center of gravity (see Table 3). The targeted C_L is achieved by repeatedly tuning the angle of attack as CFD iterations proceed. As a result, the angle of attack in the simulation is not necessarily exactly equal to the one measured during the flight test. Since deviations were found to remain within the margins of measurement accuracy (see Table 4), this was considered acceptable. Trimming is based on the C_{My} integrated from the CFD solution. The horizontal stabilizer angle is set individually for each flight condition and readjusted in every CFD-CSM iteration loop.

A finite element model with 274,500 nodes and 1.20 million degrees-of-freedom, comprising slat/flap settings for both CLEAN and FULL configurations, Fig. 8, was made available by AIRBUS Industries. The model is compliant to AM2036 quality standards and has been dynamically validated using ground vibration test data. Finite element model updating has been restricted to an adaptation of the stiffness distribution to ensure accurate results for both dynamic and static loads. The wing consists of the wing box, slats, slat tracks, inner and outer flaps, flap tracks, engines, main landing gear, ailerons, and winglet. Engines are modeled as concentrated masses and attached to the wing using general elements (GENEL) [11].

To accurately simulate free-flight conditions a free–free suspension is constituted in the static structural analyses using the

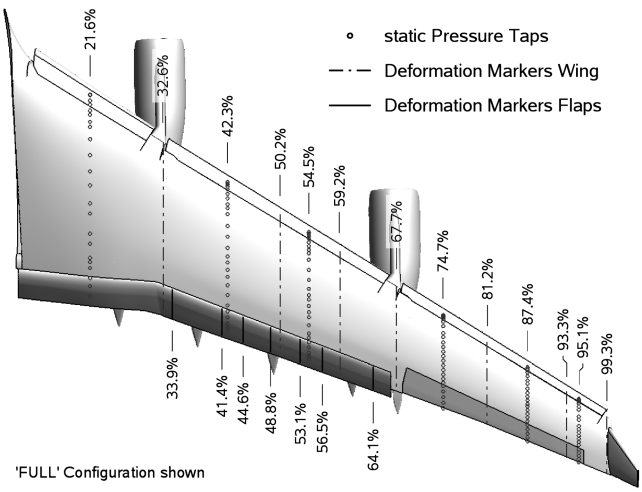

Fig. 9 Wing instrumentation.

Table 2 Estimated uncertainties of aerodynamic coefficients

Configuration:	CLEAN	FULL
Lift coefficient	± 0.015	± 0.01
Drag coefficient	$\pm 5 \times 10^{-4}$	
Pitching moment coefficient	$\pm 1.0 \times 10^{-3}$	$\pm 2.5 \times 10^{-3}$

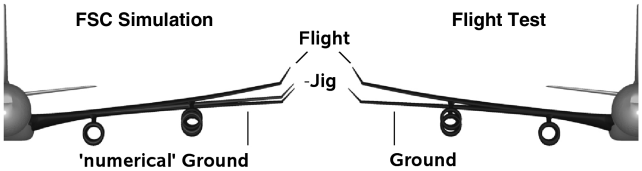

Fig. 10 Comparison of numerical and experimental deformation data (schematic).

Table 3 Validation flight-test cases for CFD-CSM coupled simulations

Number	Configuration	h_p, m	v_c, m/s	Ma	Re, $\times 10^6$	α, deg	β, deg	$p_{dyn.}$, kPa	p_s, kPa	m, t	Center of gravity, %
1	CLEAN, $Ma = 0.82$	12,508	243.0	**0.821**	35.30	2.579	−0.0446	8.40	17.90	182.7	35.7
2	CLEAN, $Ma = 0.84$	11,566	246.8	**0.841**	43.14	1.722	−0.0127	10.2	20.80	178.7	34.8
3	FULL, alpha = 5		78.16	0.235	28.99	**5.046**	0.3799	2.70		145.1	33.8
4	FULL, alpha = 10	3,051	67.98	0.204	25.07	**10.00**	−0.2068	2.00	69.70	144.7	33.6
5	FULL, alpha = 15		60.25	0.181	22.31	**15.23**	−0.3742	1.60		144.0	33.7

Table 4 Uncertainties of flight-test data

Configuration:	CLEAN	FULL
Angle of attack	±0.3 deg	
Stat. reference pressure	±30 Pa	
Pressure coefficient	$\pm 6.0 \times 10^{-4}$	$\pm 3.2 \times 10^{-3}$
Bending deformation	±50 mm	
Twist deformation	±0.1 deg	

"inertia relief" option [11] in NASTRAN™. Fuel mass is individually adjusted to the existing amount of fuel during the different flight conditions at time of data acquisition. Additionally, engine thrust values are derived from the computed C_D and introduced as discrete structural forces, equally distributed onto all four engine pivot nodes. Aerodynamic forces on the flap track fairings are applied to the respective mounting locations on the flap tracks.

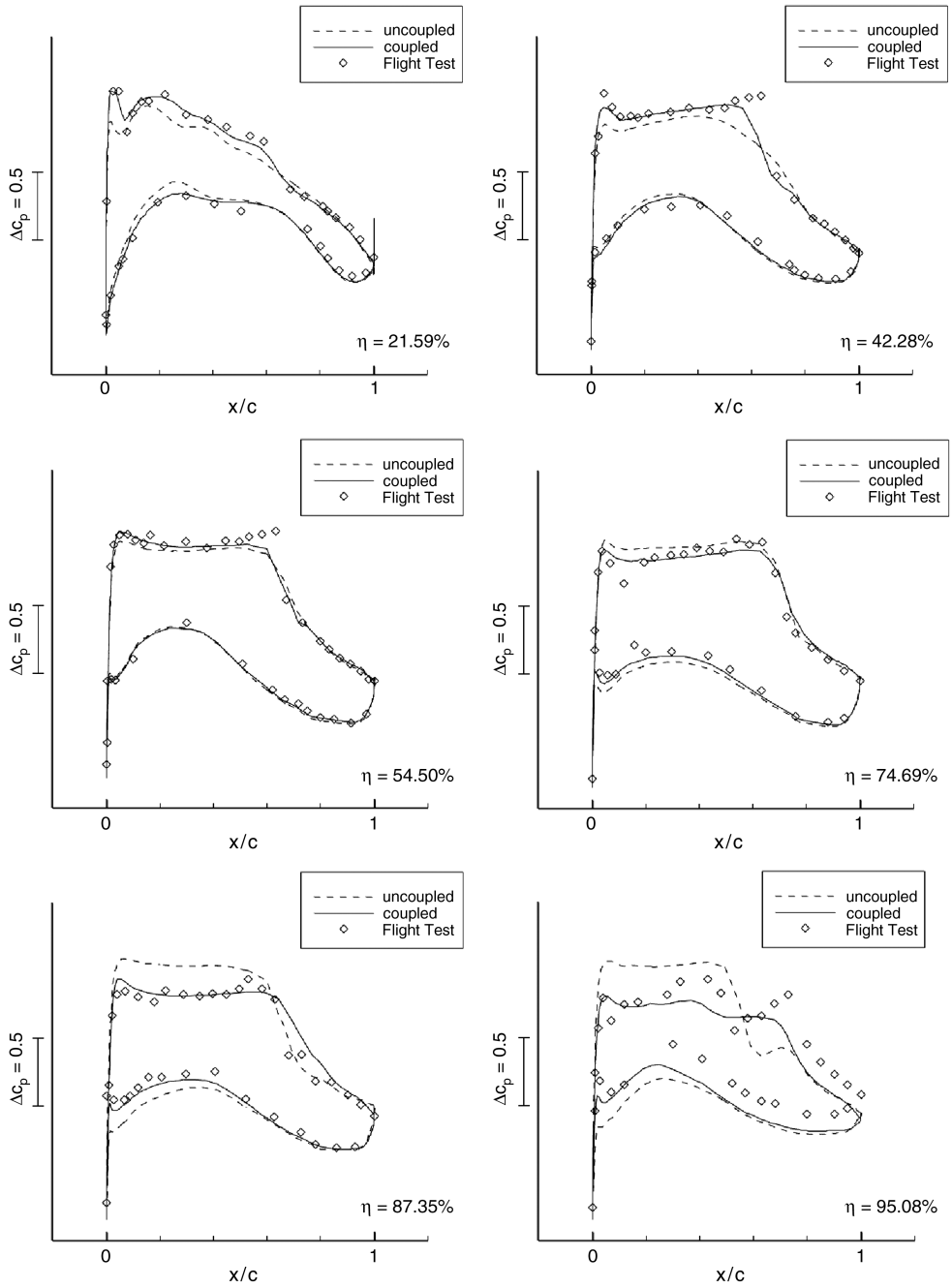

Fig. 11 Comparison of conventional and coupled CFD simulations to flight-test data, configuration CLEAN ($Ma = 0.821$).

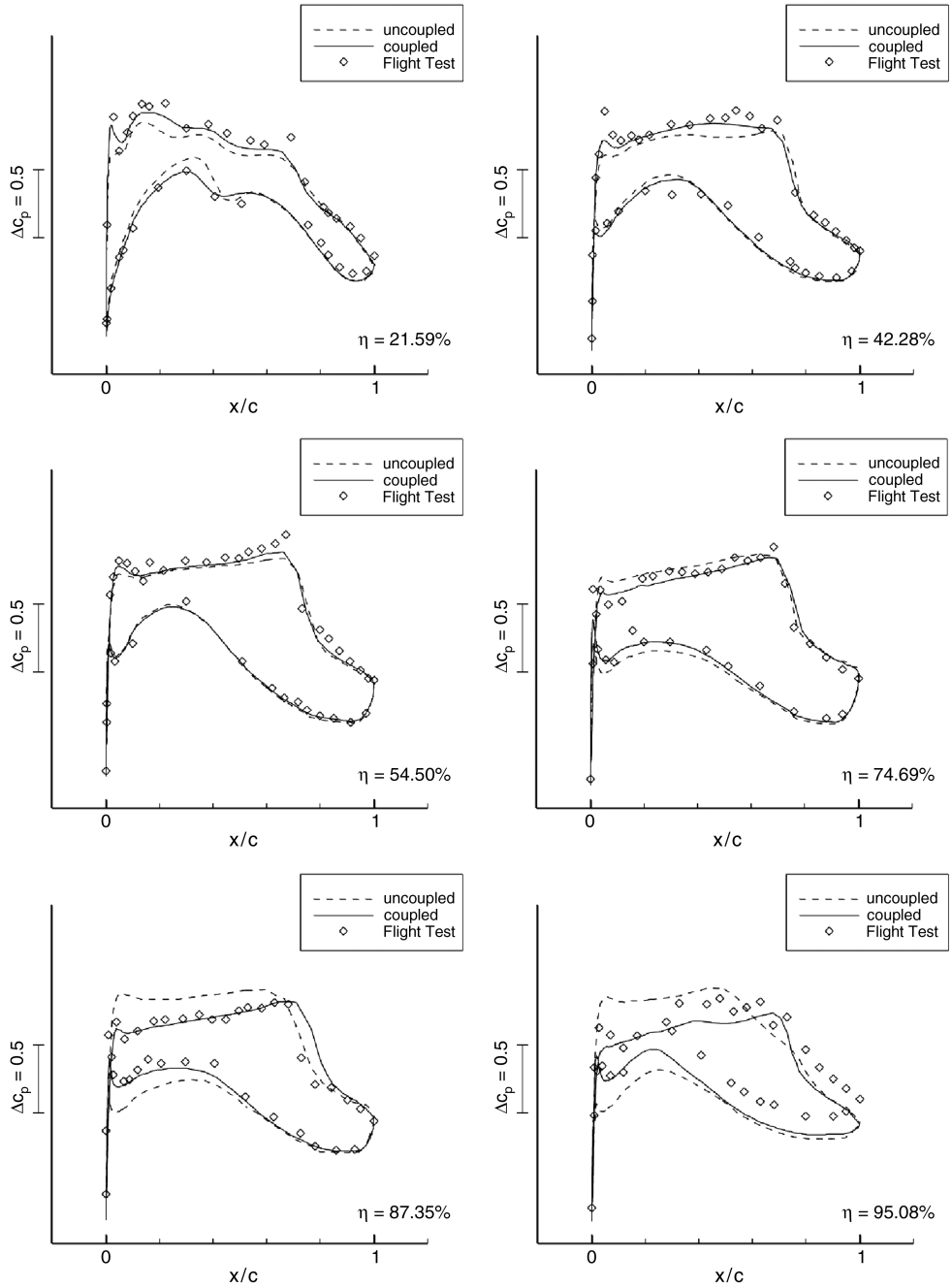

Fig. 12 Comparison of Conventional and Coupled CFD Simulations to flight-test data, configuration CLEAN ($Ma = 0.841$).

For the CLEAN wing configuration, coupling of aerodynamic loads between CFD simulation and finite element analysis is established on the main wing and winglet, using a total of approximately 197,400 surface grid points on CFD side and 2900 surface nodes in the finite element grid. With the high-lift test cases two additional, independent coupling surfaces are introduced on the leading-edge slats and trailing-edge flaps, respectively, leading to a total of 498,800 CFD surface grid points and 13,160 finite element surface nodes.

IV. Validation Data

The A340-300 used during the AWIATOR test campaigns was equipped for in-flight acquisition of wing pressure distributions and wing deformations. The instrumentation common to both CLEAN and FULL configurations includes static pressure taps in six spanwise sections between $\eta = 21.6$ and 95.1% and optical markers in seven spanwise sections between $\eta = 32.6$ and 99.3%, Fig. 9, with three targets per section to determine both bending and twist deformation components.

For testing in FULL configuration additional pressure taps were installed on slats (all sections) and flaps (sections 1–3). However, a preliminary data review revealed that pressure distributions on the inner two wing sections were not suitable for validation purposes due to insufficient long-term repeatability between the two test campaigns. Therefore, comparison of numerical and experimental data for the FULL configuration will be restricted to sections 3–6.

To determine flap deformations relative to the wing, additional deformation markers were positioned on the outer flap surface ($\eta = 33.9$–64.1%). Two digital SLR cameras inside the fuselage were used to record wing deformations using both 2-D and 3-D photogrammetry techniques. Camera 1 covered all targets, whereas camera 2 covered only the outer targets between $\eta = 50.2$ and 99.3% on the wing and $\eta = 53.1$ and 64.1% on the flap, respectively.

During all test campaigns in-flight deformation data was measured as relative deflections with respect to the ground shape as a reference.

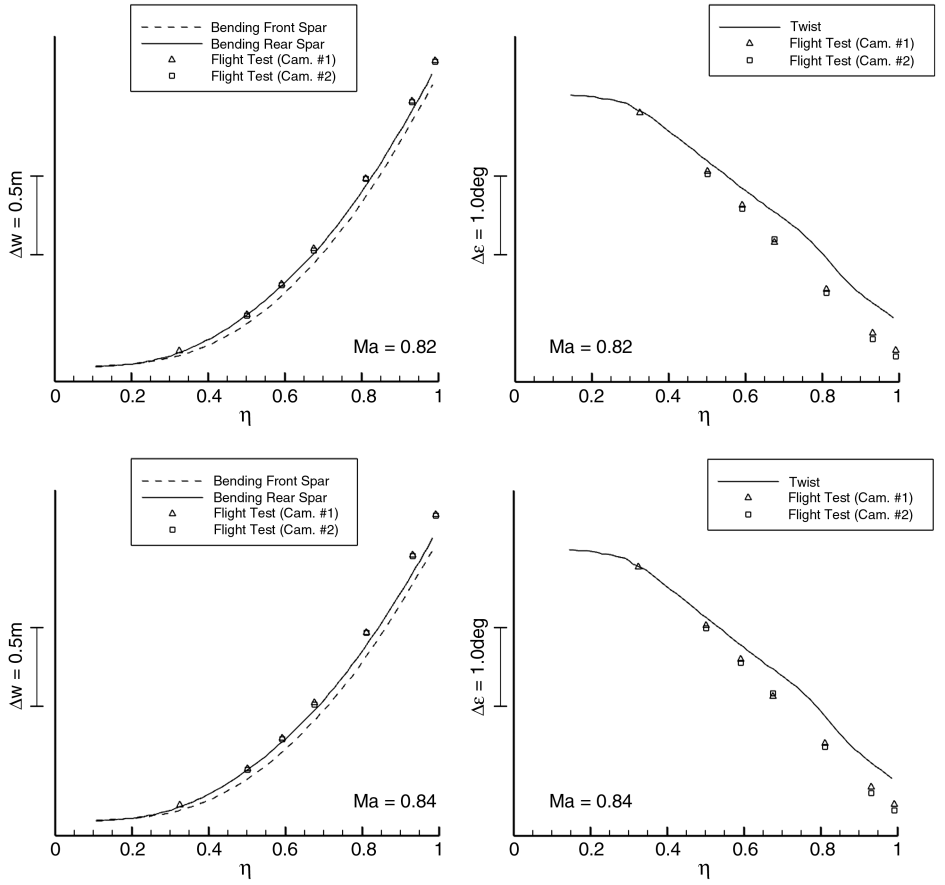

Fig. 13 Comparison of wing bending and twist deformations from fluid-structure coupled simulations to flight-test data, configuration CLEAN.

Computed deflections, in contrast, are related to the undeformed jig shape geometry, which prevents a direct comparison to measured results. The situation is sketched in Fig. 10. Among the various options available to determine the difference between jig and ground shapes, and hence enable a comparison of numerical and experimental deformation data, an additional structural analysis at 1 g loading with the aircraft suspended on main and nose landing gears and fuel mass taken into account was considered the most accurate alternative. Accordingly, all experimental and numerical deformation data presented in the following chapter will be plotted as difference between flight and ground shapes, i.e., $\Delta w = w_{\text{Flight}} - w_{\text{Ground}}$ and $\Delta\varepsilon = \varepsilon_{\text{Flight}} - \varepsilon_{\text{Ground}}$.

Two different cruise flight conditions at $Ma = 0.821$ and 0.841 and three high-lift low-speed flight states with angles of attack of $\alpha = 5$, 10, and 15 deg, respectively, were selected as validation test cases, Table 3. Main selection criteria were a sufficient variation of wing loads, yaw angles equal to or very close to zero to ensure good data quality, and the availability of both aerodynamic and structural deflection data. All experimental data was averaged over time for a variable period, depending on current fluctuation levels. Uncertainties for the AWIATOR flight-test data are listed in Table 4.

V. Results

A. CLEAN Configuration

Figures 11 and 12 show a comparison of chordwise C_p-distributions from the conventional and coupled RANS CFD simulations in trimmed condition to flight-test data for the CLEAN configuration. Generally, a better correlation to measured data is observed with the coupled results as expected. Deviations between uncoupled simulations and experimental data increase with aeroelastic deformation magnitudes towards the wing tip. Although the wing root region does not deform much, the fully coupled analysis still reveals moderately lower pressure magnitudes on the upper surface. This is due to an increase in overall angle of attack, introduced to compensate for the reduced lift in the outer wing region and to maintain constant overall lift.

Shock locations, primarily those at the outer static pressure sections, are not always precisely resolved. This is believed to be due to the underestimation of wing twist in the numerical simulations (cf. Fig. 13) and to the one-equation turbulence model used in this analysis to achieve reasonable CPU times. Some larger deviations between experimental and numerical data also occur at the outermost wing section at $\eta = 95.1\%$, which likewise may be caused by wing twist offset. Additionally, experimental data quality for this section has been found to suffer from large scatter.

In Fig. 13 spanwise wing bending and torsion deformations are plotted. While computed bending deformations match measured data reasonably well, the aerodynamically more relevant twist deflections show comparatively large differences at $\Delta\varepsilon = \varepsilon_{\text{ana.}} - \varepsilon_{\text{exp.}} =$ 0.30 deg for $Ma = 0.821$ and $\Delta\varepsilon = 0.50$ deg for $Ma = 0.841$, both values measured at wing tip. This is most likely due to the fact that aerodynamic forces on the trailing-edge control surfaces could not be precisely transferred to the corresponding locations in the structural model, as the aileron and flap structures were not modeled explicitly in the finite element model. For the analyses the model had been originally built for the according level of detail was not required. However, in the process of interpolating distributed aerodynamic loads this leads to a lower nose-down torsion moment. Other uncertainties arise from gravitational wing loads, since the exact mass distribution in the partially filled fuel tanks remains unknown.

B. FULL Configuration

With the FULL configuration flight states main interest was focused on how the fluid-structure coupled simulation approach would handle the increased complexity with respect to both CFD and structural analysis and on the aeroelastic behavior of the high-lift devices. Generally, differences between C_p-distributions for the

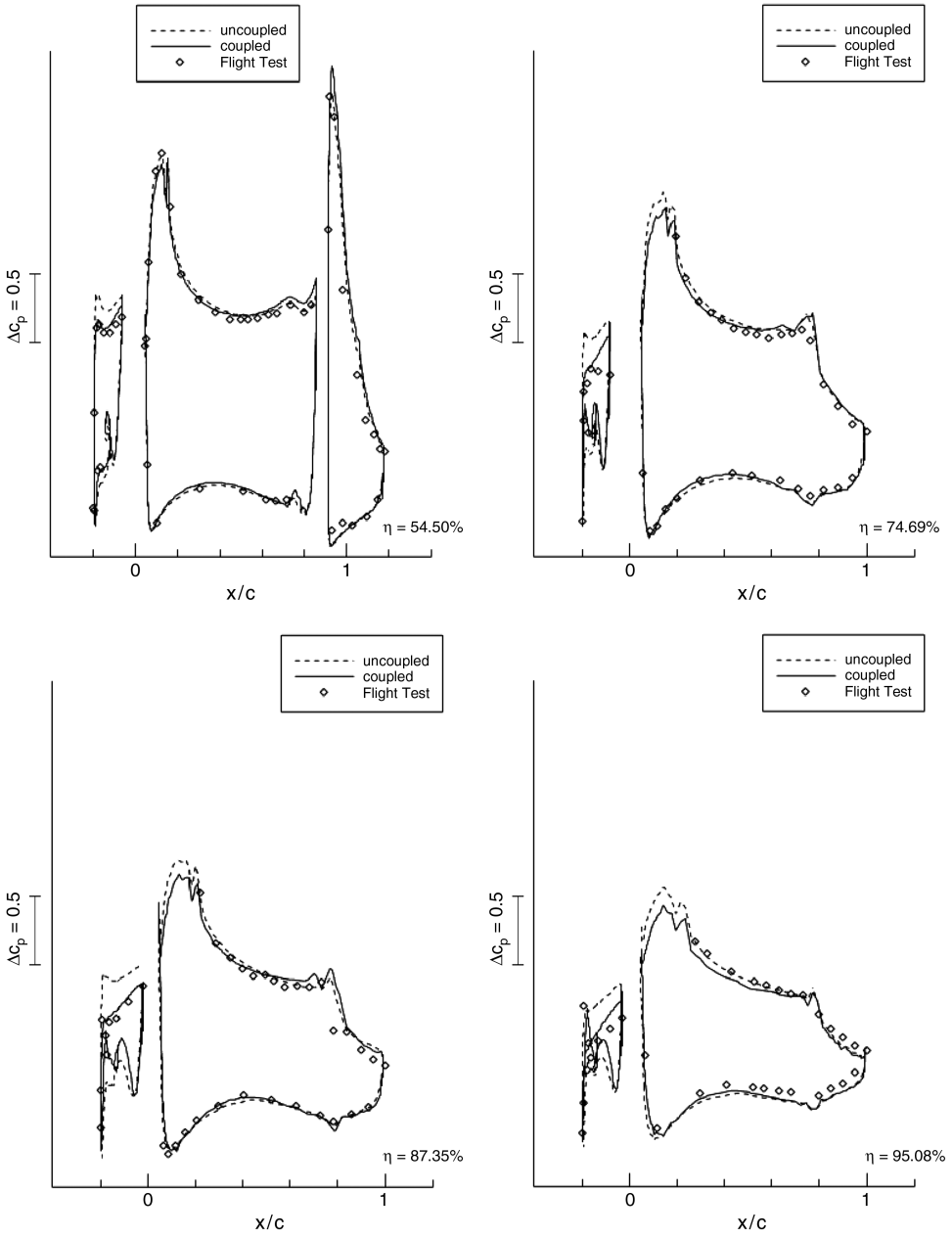

Fig. 14 Comparison of conventional and coupled simulations to flight data, configuration FULL ($\alpha = 5.046$ deg).

uncoupled and coupled simulations were found to be comparatively small as shown in Fig. 14 for $\alpha = 5$ deg. Deviations primarily occur on the upper surfaces of slat and wing, while the rear wing area and flap exhibit exceptionally small differences between fluid-structure coupled and conventional CFD solutions. In addition, deviations further decline with increasing angle of attack cf. Figs. 14 and 15. These observations have been made with other coupled high-lift simulations before [4,5] and are assumed to be mainly due to three basic phenomena:

1) At low Mach numbers the chordwise wing pressure distribution responds less sensitive to the small angle-of-attack variations caused by elastic twist deformation than under transonic flow conditions, where the high sensitivity of shock position with respect to the local angle of attack causes larger changes of the overall pressure distribution.

2) Twist deflection levels are approximately 45–60% lower, than those observed with the CLEAN cases. This is partially due to the fact, that at low Mach numbers aerodynamic loads are centered about the aeroelastic axis, leading to smaller induced torsion moments. Additionally, the total mass is approximately 20% lower than in cruise flight. Finally, in relation to the overall angles of attack the local angle-of-attack changes due to aeroelastic twist deformations are much smaller with the high-lift cases.

3) A projection of the deformed wing profile and flowfield back onto the undeformed geometry reveals, that the solutions obtained from the uncoupled and coupled simulations are essentially identical, Fig. 16, leading to virtually indistinguishable C_p-distributions in the aft wing region and on the flap. Obviously, the main wing acts like a guide vane causing the incoming flow around the flap to remain essentially unchanged, regardless of aeroelastic wing deformations. This also implies that relative deformations of the flap with respect to the wing remain small.

A close examination of the flap pressure distributions, Figs. 14 and 15, indicates that during the flight tests the flap appears to be less loaded than in the numerical simulations. This is most likely due to a simplified, and unintentionally more aerodynamic, modeling of the flap cavity cf. Fig. 16, which leads to a smaller separation, less gap flow disturbances, and higher velocities on the flap upper surface, than on the real aircraft.

Bending deformations, Fig. 17, show a good agreement between coupled simulations and flight test. For twist deformations somewhat larger deviations occur. However, considering wing chord lengths

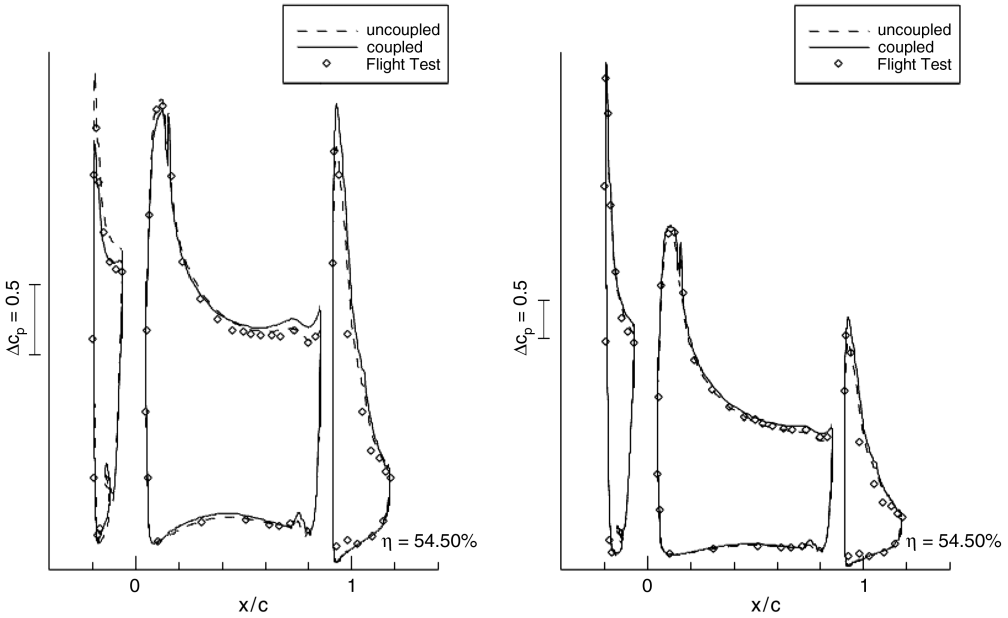

Fig. 15 Pressure distribution at wing section 3, configuration FULL ($\alpha = 10.00/15.23$ deg).

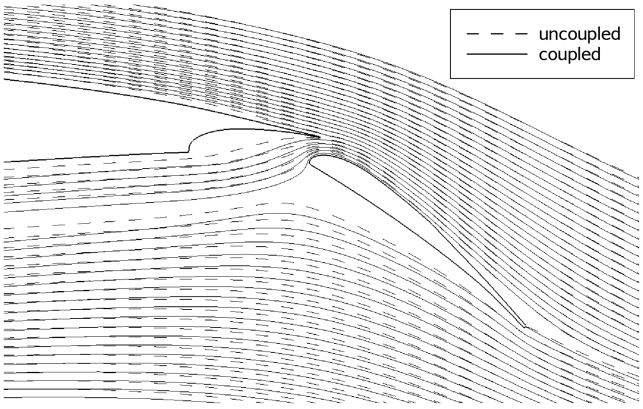

Fig. 16 Stream trace plot of flowfields around wing trailing edge and flap, $\alpha = 5.046$ deg.

these deviations are equivalent to a translational deflection error $\delta w = c \cdot \tan(\varepsilon_{\text{ana.}} - \varepsilon_{\text{exp.}}) \approx 22$ mm at wing tip, which is well within given accuracy margins (cf. Table 4).

In summary, the higher sensitivity of static wing pressure distributions and larger aeroelastic deformations make fluid-structure coupled simulations more beneficial in the transonic regime.

VI. Conclusions

The application of DLR's fluid-structure coupled simulation approach to an Airbus A340-300 transport aircraft has been described. The method uses state of the art CFD and structural analysis methods to simulate the elastically deformed aircraft at steady-state free-flight conditions, aiming at an improved estimation of aerodynamic performance and loads. No a priori knowledge of the actual flight shape is required, which allows the method to be applied to a variety of flight conditions including maneuvering operations or off-design cases. Numerical results were compared with experimental flight-test data, including both fluid dynamics and structural deflection data. Two high-speed test cases in cruise configuration and three low-speed cases in high-lift configuration were investigated.

Results for the CLEAN configuration show an improved correlation between the coupled CFD simulations and flight-test data over the conventional CFD analysis. Improvements are most significant in the wing tip region, where deformation magnitudes are large, and around the wing root, where additional lift is generated through an increased angle of attack to compensate for the lift reduction in the outer wing area. The remaining deviations with respect to shock resolution observed with both cruise flight-test cases are believed to be due to an underestimated wing twist deformation or the one-equation turbulence model used throughout these investigations. Computed wing bending and twist deformations are somewhat smaller than the measured data with larger deviations

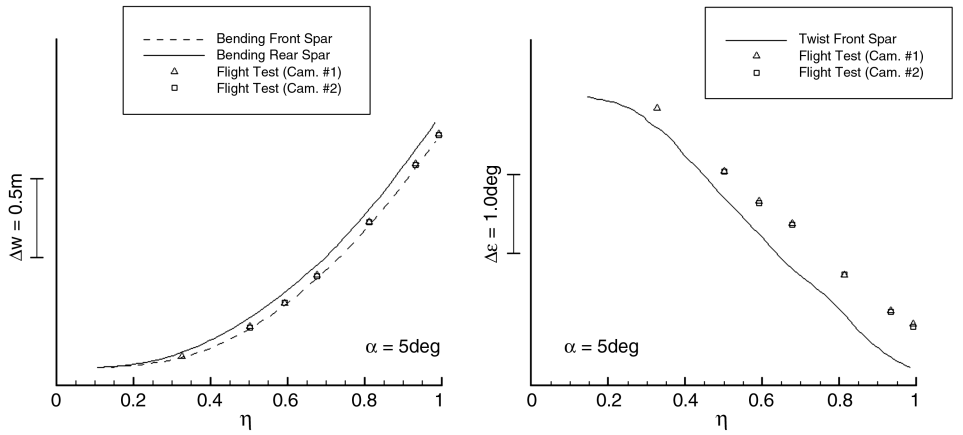

Fig. 17 Comparison of wing bending and twist deformations from fluid-structure coupled simulations to flight-test data, configuration FULL ($\alpha = 5.046$ deg).

occurring for twist. Apparently, this is caused by the missing trailing-edge control surfaces in the structural model, which affects the interpolation of aerodynamic forces, and some uncertainty regarding wing mass distribution.

With the aerodynamically and structurally more complex FULL configuration differences in static pressure distribution between the fluid-structure coupled and conventional CFD simulations remain significantly smaller than in cruise flight. Deviations are confined to the upper slat and wing surfaces and decline with increasing angle-of-attack. This is apparently due to the absence of a transonic shock, which causes a lower sensitivity of the wing pressure distribution with respect to the local angle of attack, lower overall twist deflection levels, and a guide vane effect of the main wing for the flow over the flap. Structural bending deformations show a good correlation to measured data, while twist deformations are underestimated by approximately the same extent, as found with the cruise flight cases.

Results from this and various preceding validation tests indicate that DLR's fluid-structure coupled simulation approach provides a physically correct representation of the interaction between fluid flow and flexible structure. Future applications include the integration of fuselage and horizontal/vertical tail planes to enable the aeroelastic simulation of the entire aircraft and a CFD simulation of engine intake and exhaust, which is needed for the investigation of jet-flap interactions.

Acknowledgments

This study has been funded by the German Federal Ministry of Economics and Technology within the fourth Aeronautical Research Program LuFo IV.

References

[1] Rossow, C.-C., Kroll, N., and Schwamborn, D., "Numerical Aerodynamics at DLR," *East–West High-Speed Flowfield Conference 2005*, Elsevier for the Chinese Society of Aeronautics and Astronautics, Beijing, China, Oct. 2005, pp. 31–49.

[2] Neumann, J., Nitzsche, J., and Voß, R., "Aeroelastic Analysis by Coupled Non-Linear Time Domain Simulation," *Proceedings: AVT-154 Specialists Meeting on Advanced Methods in Aeroelasticity*, NATO Research and Technology Organization, Neuilly-sur-Seine, France, May 2008, pp. 24-1–24-21.

[3] Zwaan, I. R. J., "LANN Wing Pitching Oscillations," *Compendium of Unsteady Aerodynamic Measurements*, AGARD R-702, Aug. 1982.

[4] Rudnik, R., "Towards CFD Validation for 3D High Lift Flows: EUROLIFT", *European Conference on Computational Fluid Dynamics 2001*, ECCOMAS, Swansea, United Kingdom, Sept. 2001.

[5] Heinrich, R., "Development and Application of TAU–ANSYS Coupling Procedure", *Results of the Closing Symposium of the MEGADESIGN and MegaOpt Projects*, Springer–Verlag, New York, 2009, pp. 151–168.

[6] Keye, S., Sitzmann, M., Brodersen, O., and Heinrich, R., "Fluid-Structure Coupled Loads Analysis of DLR's F6 Wing-Body Configuration", *46th AIAA Aerospace Sciences Meeting and Exhibit*, AIAA Paper 2008-0675, Jan. 2008.

[7] Heinrich, R., Kroll, N., Neumann, J., and Nagel, B., "Fluid-Structure Coupling for Aerodynamic Analysis and Design: A DLR Perspective," *46th AIAA Aerospace Sciences Meeting and Exhibit*, AIAA Paper 2008-0561, Jan. 2008.

[8] Hounjet, M. H. L., and Meijer, J. J., "Evaluation of Elastomechanical and Aerodynamic Data Transfer Methods for Non-Planar Configurations in Computational Aeroelastic Analysis," *International Forum on Aeroelasticity and Structural Dynamics*, The Royal Aeronautical Society, London, United Kingdom, June 1995.

[9] Beckert, A., and Wendland, H., "Multivariate Interpolation for Fluid-Structure Interaction Problems Using Radial Basis Functions," *Aerospace Science and Technology*, Vol. 5, No. 2, 2001, pp. 125–134. doi:10.1016/S1270-9638(00)01087-7

[10] Schwamborn, D., Gerhold, T., and Heinrich, R., "The DLR TAU-Code: Recent Applications in Research and Industry," *Proceedings of the 4th European Conference on Computational Fluid Dynamics 2006*, ECCOMAS , Delft, The Netherlands, Sept. 2006.

[11] MSC Nastran 2007r1, Quick Reference Guide, MSC Software Corporation, 2007.